

Electronic Structure of Graphene with two Strains and Double Barrier

El Bouâzzaoui Choubabi^a, Ahmed Jellal^{*a,b}, Abdellatif Kamal^a and Hocine Bahlouli^{b,c}

^a*Laboratory of Theoretical Physics, Faculty of Sciences, Chouaib Doukkali University,
PO Box 20, 24000 El Jadida, Morocco*

^b*Saudi Center for Theoretical Physics, Dhahran, Saudi Arabia*

^c*Physics Department, King Fahd University of Petroleum & Minerals,
Dhahran 31261, Saudi Arabia*

Abstract

We study the electronic structure of Dirac fermions scattered by double barrier potential in graphene under strain effect. We show that traction and compression strains can be used to generate fermion beam collimation, 1D channels, surface states and confinement. The corresponding transmission probability and conductance at zero temperature are calculated and their numerical implementations taking into account different configurations of physical parameters enabled us to analyze some features of the system.

PACS numbers: 81.05.ue, 81.07.Ta, 73.22.Pr

Keywords: graphene, strain effect, double barrier, transmission, conductance.

*a.jellal@ucd.ac.ma

1 Introduction

Recently, investigations of the strain effect on the electronic band structure, optical properties, electronic transport, spin transport and valley transport in graphene nanostructures and devices has attracted much attention from theoretical and experimental sides [1–5]. These studies were based on generalized Hamiltonian describing the quasiparticles in graphene subject to arbitrary strain effect. In particular, it turned out that the linear elasticity theory applied to graphene is a reasonable approximation for relatively small deformations, since mechanical properties demonstrate that graphene can sustain a linear elasticity regime up to 20% [6–8].

We intend to study the electronic structure of graphene ribbon deposited on a controllable silicate dioxide substrate. Such ribbon is of infinite length along the propagating x -direction of Dirac fermions with armchair boundaries (Figure 1), which is subject to two mechanical strains in two separate regions such that strain results in a contraction in one region and extension in the other. We can achieve this setting by depositing graphene onto substrates that allow the control of the strain effect [3].

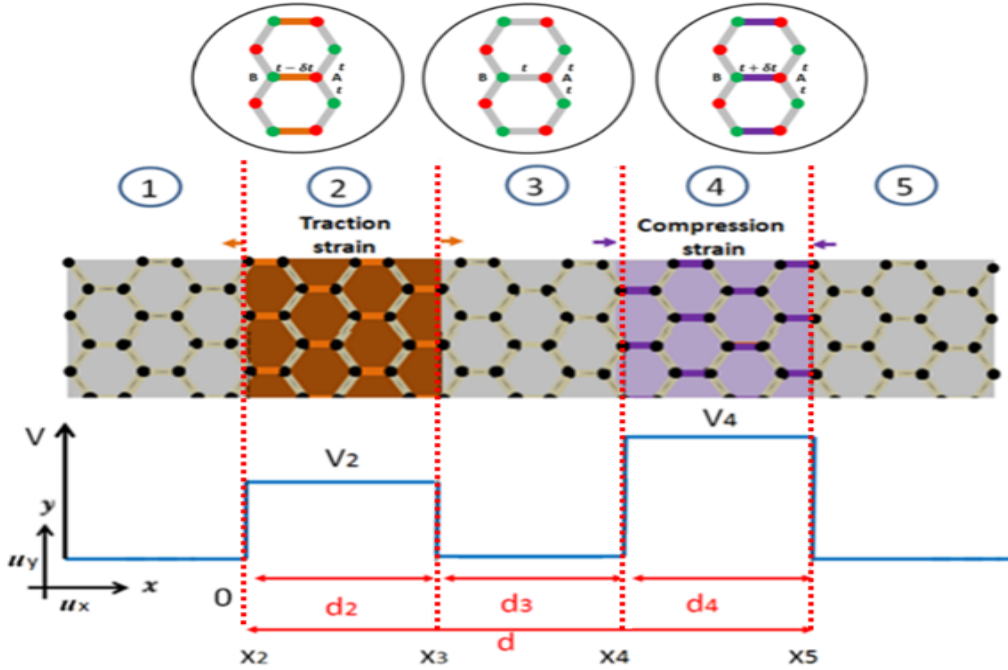


Figure 1 – (color online) Inter-carbon links for traction and compression strained graphene in the tight-binding model with $\delta t_2 = -\delta t_4 = \delta t$.

In the framework of the tight-binding model, Figure 1 shows the effect of modifying the horizontal inter-carbon bonds in the ribbon due to changes in nearest-neighbor hopping amplitude t (≈ 3 eV). The space-dependent compression and contraction influence the hopping amplitude through introducing modulations

$$t(\mathbf{R}_i, \mathbf{n}) = t + \delta t(\mathbf{R}_i, \mathbf{n}), \quad t(\mathbf{R}_i, \mathbf{n}) = t - \delta t(\mathbf{R}_i, \mathbf{n}) \quad (1)$$

where $\delta t(\mathbf{R}_i, \mathbf{n})$ is a perturbation, \mathbf{n} is the nearest neighbor vectors and \mathbf{R}_i the i -th site position. The ribbon becomes subdivided into five different regions that we index according to the positive propagation direction as ①, ②, ③, ④ and ⑤, successively. In addition to this ribbon configuration, we apply three different potentials V_2 , V_3 and V_4 in the three regions ②, ③ and ④ of width d_2 , d_3

and d_4 , respectively. The *input* and *output* regions, ① and ⑤, are made of pristine graphene and the potential is zero. The strained graphene ribbon and the profile potential constitute a double barrier of width $d = d_2 + d_3 + d_4$ as indicated in Figure 1.

The present paper is organized as follows. In section 2, we set the theoretical model and solve the eigenvalue equation to obtain the solutions of the energy spectrum. We use the boundary conditions together with the continuity equations to determine the transmission and reflection probabilities as well as the conductance in section 3. We numerically analyze the main results and present different discussions in section 4. We conclude our work in the final section.

2 Theoretical model

In strained graphene, near the valleys K and K' of the first Brillouin zone, the modification of hopping energies between different sites, through smooth perturbations, is governed by the following low energy Hamiltonian [9]

$$H = v_F \int d\mathbf{r} \Psi^\dagger \begin{bmatrix} \boldsymbol{\sigma} \cdot \left(\mathbf{p} - \frac{1}{v_F} \mathcal{A} \right) & 0 \\ 0 & -\boldsymbol{\sigma} \cdot \left(\mathbf{p} + \frac{1}{v_F} \mathcal{A} \right) \end{bmatrix} \Psi \quad (2)$$

with the momentum operator $\mathbf{p} = (p_x, p_y)$, the Fermi velocity $v_F = 3ta/2\hbar \approx 10^6 m/s$, the Pauli matrices $\boldsymbol{\sigma} = (\sigma_x, \sigma_y, \sigma_z)$, the gauge field \mathcal{A} , acting on the electrons dynamics described by a Dirac equation, and the spinor $\Psi = [\psi_K^A(\mathbf{r}), \psi_K^B(\mathbf{r}), \psi_{K'}^B(\mathbf{r}), \psi_{K'}^A(\mathbf{r})]^\dagger$. The gauge field comes from the perturbation of homogeneous amplitude jump $\delta t(\mathbf{R}, \mathbf{n})$ and they are related via

$$\mathcal{A}(\mathbf{r}) = \mathcal{A}_x(\mathbf{r}) - i\mathcal{A}_y(\mathbf{r}) = \sum_{\mathbf{n}} \delta t(\mathbf{r}, \mathbf{n}) e^{i\mathbf{K} \cdot \mathbf{n}}. \quad (3)$$

In the double barrier system, regions ② and ④ have the same width $\varrho = d_2 = d_3 = d_4$, the perturbations δt_j of horizontal hopping are constant, the index j labels the different regions and runs from 1 to 5. Such perturbations and the associated $\mathcal{A}_j(\mathbf{r})$ can be written as

$$\delta t_j(\mathbf{R}_i, \mathbf{n}) = \delta t_j \delta_{\mathbf{n},0} \theta(X_i - x_j) \theta(w - X_i + x_j) \quad (4a)$$

$$\mathcal{A}_j(\mathbf{r}) = \delta t_j \theta(x - x_j) \theta(w - x + x_j) \mathbf{u}_y. \quad (4b)$$

Note that the unit vector \mathbf{u}_y is collinear to the gauge field \mathcal{A}_j and is perpendicular to the propagating \mathbf{u}_x -direction. We can generalize the Hamiltonian to describe all regions composing our system with different couplings. Then adopting the unit system $v_F = \hbar = 1$ and allowing for the presence of an electrostatic potential $V_j(x, y)$ in the barrier region [3], the wave equations for the K valley can then be cast into

$$[-i(\partial_x - \mathcal{A}_{yj}(x)) - \partial_y - \mathcal{A}_{xj}(y)] \psi_j^B(x, y) = [E - V_j(x, y)] \psi_j^A(x, y) \quad (5a)$$

$$[-i(\partial_x + \mathcal{A}_{yj}(x)) + \partial_y - \mathcal{A}_{xj}(y)] \psi_j^A(x, y) = [E - V_j(x, y)] \psi_j^B(x, y). \quad (5b)$$

Taking into account the potential profile, translation invariance in the y -direction and using (4), we write (5) as

$$-i[(\partial_x - \delta t_j) + k_y] \varphi_j^B(x) e^{ik_y y} = [E - V_j(x)] \varphi_j^A(x) e^{ik_y y} \quad (6a)$$

$$-i[(\partial_x + \delta t_j) - k_y] \varphi_j^A(x) e^{ik_y y} = [E - V_j(x)] \varphi_j^B(x) e^{ik_y y} \quad (6b)$$

with $\psi_j^{A/B}(x, y) = \varphi_j^{A/B}(x)e^{ik_y y}$. It is convenient to introduce in j -th region the dimensionless quantities $\mathbb{V}_j = V_j/E_F$, $\varepsilon_j = E_j/E_F$, $\delta\tau_j = \delta t_j/E_F$ with $E_F = \hbar v_F/d$. Thus, the solutions in each j -region are given by

$$\psi_j(x, y) = \psi_j(x)e^{ik_y y} = w_j(x)D_j e^{ik_y y} \quad (7)$$

where the two matrices read as

$$w_j(x) = \begin{pmatrix} e^{ik_j x} & e^{-ik_j x} \\ s_j z_j e^{ik_j x} & -s_j z_j^{-1} e^{-ik_j x} \end{pmatrix}, \quad D_j = \begin{pmatrix} \alpha_j \\ \beta_j \end{pmatrix} \quad (8)$$

$\psi_j(x)$ is a spinor of components $\varphi_j^A(x)$ and $\varphi_j^B(x)$, α_j and β_j being the amplitudes of positive and negative propagation wave functions inside the j -th region, respectively. We show that the associated eigenvalues are

$$\varepsilon - \mathbb{V}_j = s_j \sqrt{(k_j d)^2 + (k_y d - \delta\tau_j)^2} \quad (9)$$

where $s_j = \text{sign}(\varepsilon - \mathbb{V}_j)$ is the usual sign function. It is clearly seen that in the energy spectrum of the j -th strained region (9), the component $k_y d$ of the wave vector is shifted by $\delta\tau_j$ compared to that of the pristine graphene. This behavior was already encountered in our previous work [10] where we had a magnetic field that also shifted the wave vector k_y by $\frac{d}{l_B^2}$, $l_B = 1/\sqrt{B_0}$ is the magnetic length and B_0 is the strength of the magnetic field. Hence from this behavior we can say that the deformation (strain effect) behaves like an effective magnetic field, and the two shifts play the role of a mass term.

3 Transmission and conductance

To determine the transmission probability, we use the boundary conditions applied successively at the interfaces along the x -direction and evaluate the current densities in the incident, reflected and transmitted regions. Indeed, at interfaces $x_j = j\varrho$, we obtain the transfer matrix $D_j = M_j D_{j+1}$ with the matrix

$$M_j = \begin{pmatrix} e^{ik_j j\varrho} & e^{-ik_j j\varrho} \\ s_j z_j e^{ik_j j\varrho} & -s_j z_j^{-1} e^{-ik_j j\varrho} \end{pmatrix}^{-1} \begin{pmatrix} e^{ik_{j+1} j\varrho} & e^{-ik_{j+1} j\varrho} \\ s_{j+1} z_{j+1} e^{ik_{j+1} j\varrho} & -s_{j+1} z_{j+1}^{-1} e^{-ik_{j+1} j\varrho} \end{pmatrix} \quad (10)$$

and we have

$$k_j = \frac{1}{d} \sqrt{(\varepsilon - \mathbb{V}_j)^2 - (k_y d - \delta\tau_j)^2}, \quad z_j = \frac{k_j - i \left(k_y - \frac{\delta\tau_j}{d} \right)}{\sqrt{k_j^2 + \left(k_y - \frac{\delta\tau_j}{d} \right)^2}}. \quad (11)$$

with $d = 3\varrho$, $s_1 = s_5$, $k_1 = k_5$, $z_1 = z_5$, $\delta\tau_j = (0, \delta\tau_2, 0, \delta\tau_4, 0)$ and $\mathbb{V}_j = (0, \mathbb{V}_2, 0, \mathbb{V}_4, 0)$. After some lengthy algebras, we obtain the transfer matrix

$$M = M_1 M_2 M_3 M_4 = \begin{pmatrix} M_{11} & M_{12} \\ M_{11} & M_{12} \end{pmatrix} \quad (12)$$

Since the incident and reflected amplitudes are defined by

$$D_1 = \begin{pmatrix} 1 \\ r \end{pmatrix}, \quad D_5 = \begin{pmatrix} t \\ 0 \end{pmatrix} \quad (13)$$

then the wavefunctions in the *input* and *output* regions are connected by the matrix M as

$$D_1 = MD_5. \quad (14)$$

On the other hand, the eigenspinors $\psi_j(x)$, appearing in (7), can be decomposed as

$$\psi_j(x) = \alpha_j \psi_j^+(x) + \beta_j \psi_j^-(x) \quad (15)$$

where the two components are given by

$$\psi_j^+(x) = \begin{pmatrix} 1 \\ s_j z_j \end{pmatrix} e^{ik_j x}, \quad \psi_j^-(x) = \begin{pmatrix} 1 \\ -s_j z_j^{-1} \end{pmatrix} e^{-ik_j x} \quad (16)$$

which are the positive and negative propagating spinors associated to their amplitudes α_j and β_j , respectively. In *input* region, conservation of the mode k_y gives the relation

$$\sin \theta_j = \frac{1}{|\varepsilon - \mathbb{V}_j|} (\varepsilon \sin \theta - \delta \tau_j) \quad (17)$$

where θ_j is the angle of propagation of Dirac fermions within j -region, $\theta = \theta_1$ is the incident angle and ε is the incident energy. From (17) we notice that the strain directly affects the transmission angle of Dirac fermions [11].

At this stage, we can introduce the current density corresponding to our system. Indeed, we show that the incident, reflected and transmitted current densities can be written as

$$J_x^{\text{in}} = \psi_1^+(x)^\dagger \sigma_x \psi_1^+(x) = 2s_1 \frac{k_1}{\sqrt{k_1^2 + k_y^2}} \quad (18a)$$

$$J_x^{\text{re}} = \psi_1^-(x)^\dagger \sigma_x \psi_1^-(x) = 2s_1 |r|^2 \frac{k_1}{\sqrt{k_1^2 + k_y^2}} \quad (18b)$$

$$J_x^{\text{tr}} = \psi_5^+(x)^\dagger \sigma_x \psi_5^+(x) = 2s_5 |t|^2 \frac{k_5}{\sqrt{k_5^2 + k_y^2}} \quad (18c)$$

giving rise to the transmission and reflection probabilities

$$T = \frac{|J_x^{\text{tr}}|}{|J_x^{\text{in}}|} = \frac{s_5 k_5}{s_1 k_1} \frac{\sqrt{k_1^2 + k_y^2}}{\sqrt{k_5^2 + k_y^2}} |t|^2, \quad R = \frac{|J_x^{\text{re}}|}{|J_x^{\text{in}}|} = |r|^2. \quad (19)$$

Due to the symmetry of the double barrier configuration in the *input* and *output* regions, we have the relations $s_1 = s_5$ and $k_1 = k_5$. Thus, using (14) to obtain

$$T = |t|^2 = \frac{1}{|M_{11}|^2}. \quad (20)$$

Since the transmission probability T is determined for each mode k_y , then we derive the conductance G at zero temperature. Indeed, using the definition [12] we find the conductance in the unit systems

$$G = \frac{2e^2}{\pi} \int_{-E}^E T_n(E, k_y) \frac{dk_y}{2\pi/L_y} \quad (21)$$

$$= G_0 \int_{-\pi/2}^{\pi/2} T_n(\varepsilon, \theta) \cos \theta d\theta \quad (22)$$

where L_y is the sample size along the y -direction and $G_0 = \frac{e^2 \varepsilon L_y}{\pi^2 d}$ is the unit conductance, d is the total barrier width. These results will numerically be investigated to analyze the system behavior and underline its basic features.

4 Results and discussions

In the beginning we analyze only the double strain effects on the graphene systems, which means that we keep strain parameter in two regions ((2), (4)) and forget about the double barrier potential $\mathbb{V}_2 = \mathbb{V}_4 = 0$. Note that, the conservation imposes $k_1 = k_3 = k_5$, $s_1 = s_3 = s_5$, which will be considered in the forthcoming analysis.

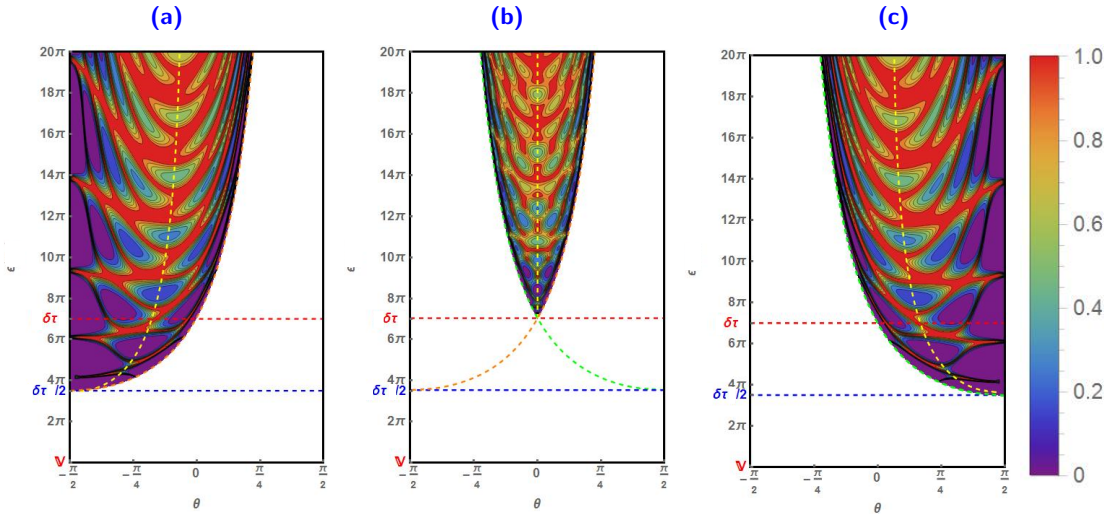


Figure 2 – (color online) Density plot of transmission probability T versus incident energy ε and incident angle θ with $\mathbb{V}_2 = \mathbb{V}_4 = 0$, $\varrho = 300$, $d = 3\varrho$, $\delta\tau = 7\pi$ (red dashed line), $\frac{\delta\tau}{2} = \frac{7\pi}{2}$ (blue dashed line), $\varepsilon = \frac{\delta\tau}{1+\sin\theta}$ (green dashed line), $\varepsilon = \frac{\delta\tau}{1-\sin\theta}$ (orange dashed line) and the symmetry curve (yellow dashed line), for (a): $\delta\tau_2 = \delta\tau_4 = -\delta\tau$, (b): $\delta\tau_2 = -\delta\tau_4 = \pm\delta\tau$, (c): $\delta\tau_2 = \delta\tau_4 = \delta\tau$.

In Figure 2, we present density plots of transmission probability as function of incident energy ε and incident angle θ . We show that the white zones that are limited in Figure 2(a) by $\varepsilon = \frac{\delta\tau}{1-\sin\theta}$ (orange dashed line), in Figure 2(b) by $\varepsilon = \frac{\delta\tau}{1-\sin\theta}$ and $\varepsilon = \frac{\delta\tau}{1+\sin\theta}$ (green dashed line), and in Figure 2(c) by $\varepsilon = \frac{\delta\tau}{1+\sin\theta}$ represent forbidden zones (FZs). Otherwise, the FZs are determined by angles $\theta = \arcsin\left(\frac{\pm(\varepsilon-\delta\tau)}{\varepsilon}\right)$, which give rise to a phenomenon resembling beam collimation in optics. These relations can be obtained either from Figure 3 (see below) or directly from the conservation of the mode k_y (17). We notice that the tunneling effect is always completely suppressed: in Figures (2(a), 2(c)) if $\varepsilon < \frac{\delta\tau}{2}$ (dashed line) which was found in the case of a single barrier [3], and in Figure 2(b) if $\varepsilon < \delta\tau$ (red dashed line) corresponding to the two collimations generated mutually by contraction and compression strains. Figure 2 tells us that the Klein paradox does not always exist at normal incidence angle $\theta = 0$. Furthermore, the transmission is not symmetrical with respect to the normal incidence angle in Figures (2(a), 2(c)), but it restores its symmetry in Figure 2(b). Note that in Figure 2 the dashed yellow line is a symmetry curve of transmission. We observe that in Figure 2(b) there is a perfect symmetry, on the other in Figures (2(a), 2(c)) there is absence of symmetry. In Figures 2,

purple zones represent transmission gaps ($T = 0$) and red zones represent total transmission ($T = 1$) i.e. Klein tunneling effect. Inspecting the last Figures, exposes the following symmetry relations

$$T(\theta, \delta\tau, \delta\tau) = T(-\theta, -\delta\tau, -\delta\tau) \quad (23a)$$

$$T(\theta, \delta\tau, -\delta\tau) = T(\theta, -\delta\tau, \delta\tau) \quad (23b)$$

$$T(\theta, \pm\delta\tau, \mp\delta\tau) = T(-\theta, \pm\delta\tau, \mp\delta\tau). \quad (23c)$$

Collimation is due to filtering effect at certain incidence angles, Figure 3 shows this effect which is best understood by inspecting the phase-spaces [3]. The Fermi surface of pristine graphene is highlighted in yellow and has a dispersion given by $\varepsilon^2 = d^2(k_x^2 + k_y^2)$. The strained graphene, on the other hand, exposes a green and orange Fermi surface for compression and contraction strain whose equations are, respectively,

$$\varepsilon^2 = d^2k_{2,4}^2 + (dk_y + \delta\tau)^2, \quad \varepsilon^2 = d^2k_{2,4}^2 + (dk_y - \delta\tau)^2. \quad (24)$$

Conservation of energy and momentum k_y immediately leads to a sector of allowed incident angles (red surfaces) whose openings are limited by the red arrows in Figure 3 and corresponding exactly to the allowed incident angles shown in Figure 2. If $\delta\tau$ exceeds 2ε , the red surface will be omitted and therefore tunneling in strained double barrier is suppressed. Figures (3(a), 3(c)) show that the two red surfaces are symmetric with respect to the normal incidence angle but in Figure 3(b) the red surface is symmetric with respect to the normal incidence angle. By combining Figures (2, 3) we can explain easily the Dirac fermions like collimation in strained double barrier.

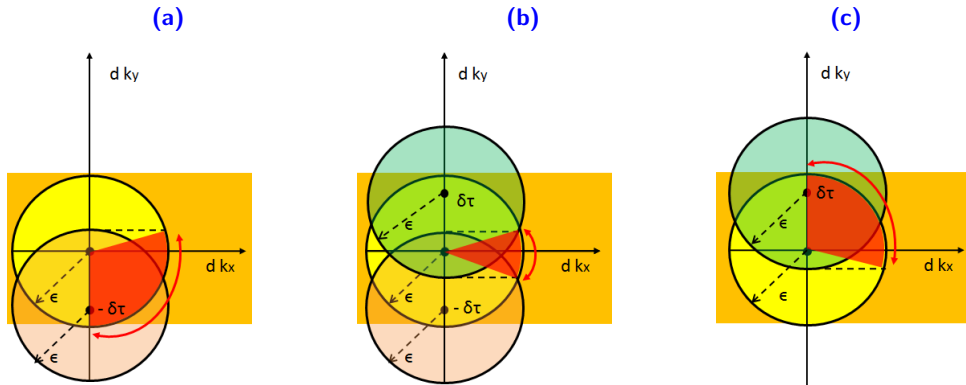


Figure 3 – (color online) Fermi surfaces affected by strain in double barrier, for (a): $\delta\tau_2 = \delta\tau_4 = -\delta\tau$, (b): $\delta\tau_2 = -\delta\tau_4 = \pm\delta\tau$, (c): $\delta\tau_2 = \delta\tau_4 = \delta\tau$.

Considering the symmetry between $T(\theta, \delta\tau, \delta\tau)$ and $T(\theta, -\delta\tau, -\delta\tau)$ with respect to $\theta = 0$, we will only study $(T(\theta, \delta\tau, \delta\tau), T(\theta, \delta\tau, 0))$ and deduce the other symmetrical cases. In Figure 4, we evaluate the transmission difference between a strained single barrier with $(\delta\tau_2 = \delta\tau, \delta\tau_4 = 0)$ and the strained double barrier with $(\delta\tau_2 = \delta\tau_4 = \delta\tau)$, the two Figures (4(a), 4(b)) have the same white forbidden zone and therefore the same allowed incident angles. The double barrier introduces a radical change as compared to in single barrier transmission. In Figure 4(a) the single barrier is not symmetrical (no yellow curve), it possess separate total energy bands (red color) having parabolic form that start with peaks at grazing incidence $\theta = \frac{\pi}{2}$ for $\delta\tau$ ($\theta = -\frac{\pi}{2}$ for $-\delta\tau$), these peaks are intercalated by

transmission gaps (purple zones). The first transmission gap starts its location between energy $\frac{\delta\tau}{2}$ (blue dashed line) and first peak, it coats the transmission density plot on the green dashed line side $\varepsilon = \frac{\delta\tau}{1+\sin\theta}$ and becomes thin when the energy increases. Transmission gaps between peaks decreases in width (compared to θ) and increases in height (compared to ε) when the energy increases. The double barrier effect is explained in Figure 4(b), the density plot has a symmetry deformed with respect to the yellow line. Indeed the total transmission bands (red zones) become fragmented and contain islands of different transmission values, transmission gaps intercalated between the peaks (at the grazing angle) are duplicated and asymmetric with respect to the yellow line, and the peaks are duplicated and asymmetric as well. We observe that the energy $\varepsilon = \frac{\delta\tau}{2}$ plays the role of mass term whose lower energy is forbidden. In the presence of a mass term comes the first transmission gap followed by the first peak.

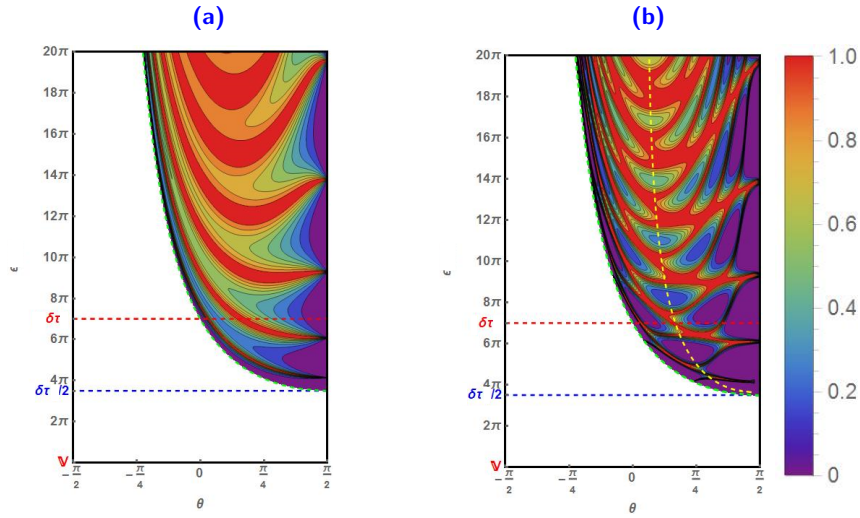


Figure 4 – (color online) Density plot of transmission probability T versus incident energy ε and incident angle θ with $\mathbb{V}_2 = \mathbb{V}_4 = 0$, $\varrho = 3\varrho$, $d = 3\varrho$, $\delta\tau = 7\pi$ (red dashed line), $\frac{\delta\tau}{2} = \frac{7\pi}{2}$ (blue dashed line), $\varepsilon = \frac{\delta\tau}{1+\sin\theta}$ (green dashed line) and the symmetry curve (yellow dashed line). (a): Strained single barrier with $\delta\tau_2 = \delta\tau$, $\delta\tau_4 = 0$. (b): Strained double barrier with $\delta\tau_2 = \delta\tau_4 = \delta\tau = 0$.

To show difference between peaks behavior of the transmissions in strained single and double barriers at the grazing incidence angle $\theta = \frac{\pi}{2}$ for $\delta\tau$ ($\theta = -\frac{\pi}{2}$ for $-\delta\tau$), we present Figure 5 with the same conditions as in Figure 4. In Figure 5(a), the transmission probability T versus incident energy ε at grazing incidence θ contains a series of peaks intercalated with transmission gaps that increase as ε increases. In Figure 5(b), T behaves like the one in the Figure 5(a) but with double resonance peaks, the separation between peak doublet increases also with energy. Such resonance peaks can easily be explained by the doubling of the resonator model of Fabry-Perot in graphene [13–15]. The two barrier types (single and double) have no effect on the width of the transmission gaps between transmission peaks. Figure 5 shows also the forbidden transmission zone between the zero energy $\varepsilon = 0$ and the mass-like term $\frac{\delta\tau}{2}$.

Figure 6 shows the transmission density plot versus incident energy ε and deformation $\delta\tau$ where white zones correspond to forbidden transmission, purple zones correspond to transmission gaps and red zones correspond to total transmission. The allowed transmission corresponds to the energies

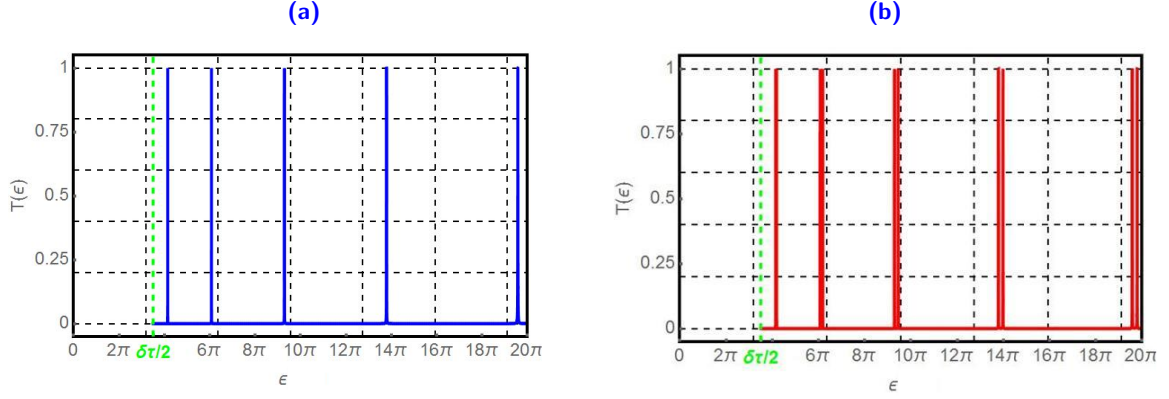


Figure 5 – (color online) Transmission probability T versus incident energy ε at grazing incidence $\theta = \pm\frac{\pi}{2}$ with $\mathbb{V}_2 = \mathbb{V}_4 = 0$, $\varrho = 300$, $d = 3\varrho$, $\delta\tau = 7\pi$ (green dashed line). (a): Strained single barrier with $\delta\tau_2 = \pm\delta\tau, \delta\tau_3 = \delta\tau_4 = 0$. (b): Strained double barrier with $\delta\tau_2 = \pm\delta\tau_4 = \pm\delta\tau$.

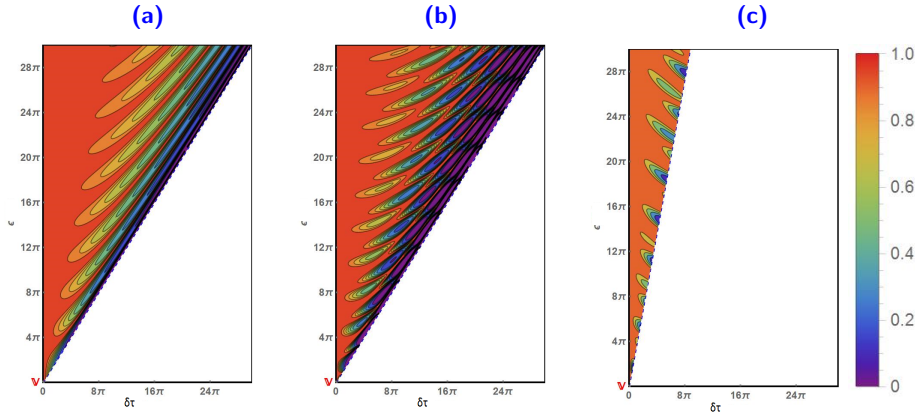


Figure 6 – (color online) Density plot of transmission probability T versus incident energy ε and $\delta\tau$ with $\mathbb{V}_2 = \mathbb{V}_4 = 0$, $\varrho = 300$, $d = 3\varrho$. (a): Single barrier transmission density plot in normal incidence with $\delta\tau_2 = \pm\delta\tau, \delta\tau_4 = 0$ or $\delta\tau_2 = 0, \delta\tau_4 = \pm\delta\tau$. (b): Double barrier transmission density plot in normal incidence with $\delta\tau_2 = -\delta\tau_4 = \pm\delta\tau$. (c): Double barrier transmission density plot in incident angle $\theta = \frac{\pi}{4}$ with $\delta\tau_2 = -\delta\tau_4 = \pm\delta\tau$.

$\varepsilon \geq \frac{\delta\tau}{1-\sin\theta}$. In Figures (6(a), 6(b)), the single and double barrier transmissions are illustrated respectively at normal incidence $\theta = 0$, we observe that near $\delta\tau = 0$ (i.e. the pristine graphene is slightly deformed) always there is the effect of Klein paradox (red color). As long as the deformation increases, the different transmission values appear and we end up with transmission gaps just before the energy $\varepsilon = \frac{\delta\tau}{1-\sin\theta}$. The contribution of the double barrier compared to the single one is marked by the appearance of the islands of transmissions, which are surrounded by total transmission zones and multiplication of transmission gap zones on the sides of $\varepsilon = \frac{\delta\tau}{1-\sin\theta}$. The number of these islands and transmission gaps increase as long as energy increases. Figure 6(c) ($\theta = \frac{\pi}{4}$) shows that if the angle of incidence increases the forbidden zone increases, islands and transmission gaps decrease, which telling us the system behaves like a slightly strained pristine graphene.

Beside the strained graphene, a symmetrical potential profile $(\mathbb{V}_2, \mathbb{V}_4) = (\mathbb{V}, \mathbb{V})$ has been applied to study its additional effect compounded to that of strain. Figure 7 shows the transmission density plot versus incident energy ε and incident angle θ . The allowed transmissions correspond, respectively

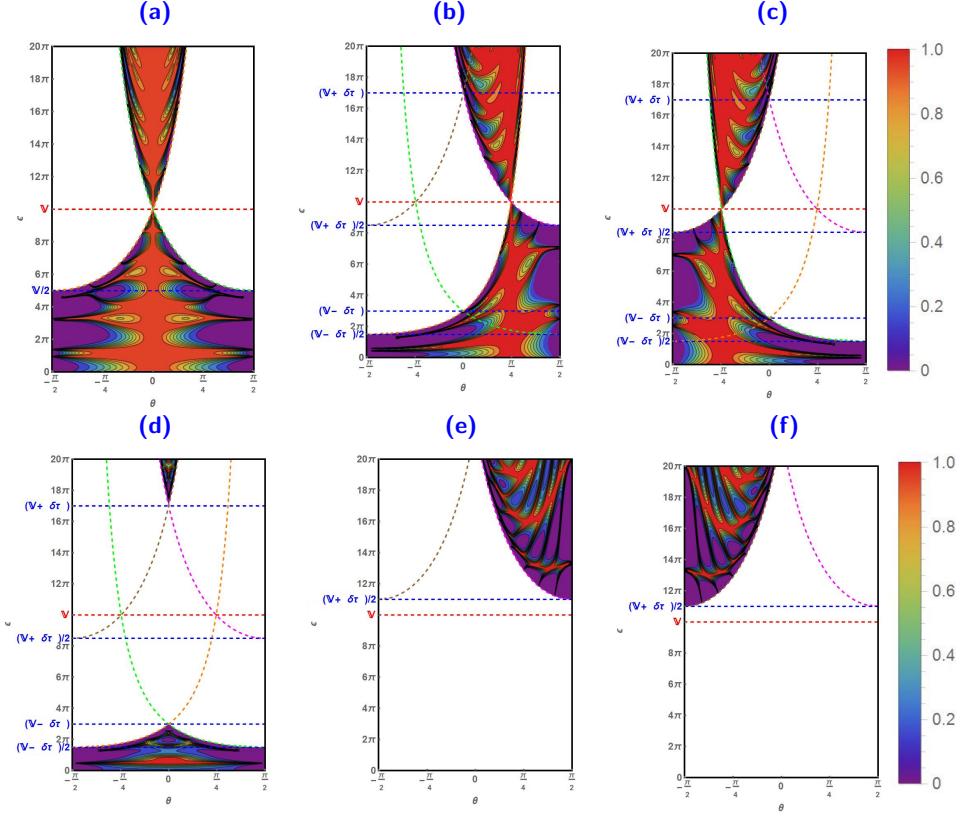


Figure 7 – (color online) Density plot of transmission probability T versus incident energy ε and incident angle θ with $\mathbb{V}_2 = \mathbb{V}_4 = \mathbb{V} = 10\pi$, $\varrho = 300$, $d = 3\varrho$, $\mathbb{V} = 10\pi$ (red dashed line), $(\frac{\mathbb{V} \pm \delta\tau}{2}, \mathbb{V} \pm \delta\tau)$ (blue dashed lines), $\varepsilon_{\pm}^{\pm} = \frac{\mathbb{V} + \delta\tau}{1 \pm \sin\theta}$ (brown dashed line), $\varepsilon_{\pm}^{\pm} = \frac{\mathbb{V} + \delta\tau}{1 + \sin\theta}$ (magenta dashed line), $\varepsilon_{\pm}^{\pm} = \frac{\mathbb{V} - \delta\tau}{1 - \sin\theta}$ (orange dashed line), $\varepsilon_{\pm}^{\pm} = \frac{\mathbb{V} - \delta\tau}{1 + \sin\theta}$ (green dashed line). (a): $\delta\tau_2 = \delta\tau_4 = \delta\tau = 0$. (b): $\delta\tau_2 = \delta\tau_4 = \delta\tau = 7\pi$. (c): $\delta\tau_2 = \delta\tau_4 = \delta\tau = -7\pi$. (d): $\delta\tau_2 = -\delta\tau_4 = \delta\tau = \pm 7\pi$. (e): $\delta\tau_2 = \delta\tau_4 = \delta\tau = 12\pi$ and $\delta\tau > \mathbb{V}$. (f): $\delta\tau_2 = \delta\tau_4 = \delta\tau = -12\pi$ and $\delta\tau > \mathbb{V}$.

to the energy zones: $[\varepsilon \geq (\varepsilon_{-}^{+} = \varepsilon_{-}^{-}) \wedge \varepsilon \geq (\varepsilon_{-}^{+} = \varepsilon_{-}^{-})] \vee [\varepsilon \leq (\varepsilon_{-}^{+} = \varepsilon_{-}^{-}) \wedge \varepsilon \leq (\varepsilon_{-}^{+} = \varepsilon_{-}^{-})]$ Figure 7(a), $[\varepsilon \geq \varepsilon_{-}^{-} \wedge \varepsilon \geq \varepsilon_{+}^{+}] \vee [\varepsilon \leq \varepsilon_{-}^{-} \wedge \varepsilon \leq \varepsilon_{+}^{+}]$ Figure 7(b), $[\varepsilon \geq \varepsilon_{+}^{+} \wedge \varepsilon \geq \varepsilon_{-}^{-}] \vee [\varepsilon \leq \varepsilon_{+}^{+} \wedge \varepsilon \leq \varepsilon_{-}^{-}]$ Figure 7(c), $[\varepsilon \geq \varepsilon_{+}^{+} \wedge \varepsilon \geq \varepsilon_{-}^{-}] \vee [\varepsilon \leq \varepsilon_{+}^{+} \wedge \varepsilon \leq \varepsilon_{-}^{-}]$ Figure 7(d), $[\varepsilon \geq \varepsilon_{+}^{+}]$ Figure 7(e), and $[\varepsilon \geq \varepsilon_{+}^{+}]$ Figure 7(f). The forbidden transmission zones (white color) correspond respectively to the complementary allowed transmission zones in each systems as illustrated in Figure 7, with $\varepsilon_{+}^{\pm} = \frac{\mathbb{V} \pm \delta\tau}{1 \pm \sin\theta}$ and $\varepsilon_{-}^{\pm} = \frac{\mathbb{V} \pm \delta\tau}{1 - \sin\theta}$. Figure 7(a) shows the transmission probability $T(\varepsilon, \theta)$ for a strainless double barrier with potential ($\mathbb{V}_2 = \mathbb{V}$), the energy spectrum is subdivided into three energy domains. The first domain is $0 \leq \varepsilon \leq \frac{\mathbb{V}}{2}$ where the transmission is allowed for all incidence angles $-\frac{\pi}{2} \leq \theta \leq \frac{\pi}{2}$, the double barrier behaves as a more refractive medium than pristine graphene. The second domain is $\frac{\mathbb{V}}{2} \leq \varepsilon \leq \mathbb{V}$, which shows that at each energy there are two critical angles symmetrical with respect to the normal incidence, they come closer when the energy tends to \mathbb{V} . The third domain corresponds to $\varepsilon \geq \mathbb{V}$, when the energy increases the critical angles remain always symmetrical but they move away parabolically. In the two last domains, the double barrier behaves like a less refractive medium than pristine graphene. In vicinity of normal incidence, we have a total transmission (red color) whatever the propagating energy of Dirac fermions (Klein Paradox). The transmission probability is symmetrical with respect to normal incidence angle $\theta = 0$, it vanishes when approaching the limit angles to give transmission

gaps (purple color) intercalated between resonance peaks. The transmission, in Figure 7(a), has the same form as that obtained by the transmission through a potential barrier in monolayer graphene studied in [16]. In Figures 7(b), 7(c)), we illustrate the double barrier, which becomes strained by adding $(\delta\tau_2 = \delta\tau_4 = \delta\tau = 7\pi, \delta\tau < \mathbb{V})$ and $(\delta\tau_2 = \delta\tau_4 = \delta\tau = -7\pi, \delta\tau < \mathbb{V})$, respectively. With respect to normal incidence, the two transmissions in these last two Figures are symmetrical to each other, the transmission lose its symmetry (as compared to Figure 7(a)) with respect to the normal incidence. The transmission has an additional domain compared to that of strainless double barrier, which just appeared between the first and the second zones. In this domain, the transmission in 7(b) (7(c)) is allowed in the positive (negative) incidence $\theta > 0$ ($\theta < 0$) and limited by critical angles in the negative (positive) incidence $\theta < 0$ ($\theta > 0$). In Figures 7(e), 7(f)) plotted for $(\delta\tau_2 = \delta\tau_4 = \delta\tau = 12\pi, \delta\tau > \mathbb{V})$ and $(\delta\tau_2 = \delta\tau_4 = \delta\tau = -12\pi, \delta\tau > \mathbb{V})$, respectively, there remains only one transmission domain for energies $\varepsilon > \frac{\mathbb{V} + \delta\tau}{2}$. The system behaves as a strained double barrier, with no potential profile, with a like compression strain $\delta\tau' = \mathbb{V} + \delta\tau$. Figure 7(d) for a double barrier composed by compression and traction $(\delta\tau_2 = -\delta\tau_4 = \delta\tau = \pm 7\pi)$ with a predicted potential $(\mathbb{V}_2, \mathbb{V}_4) = (\mathbb{V}, \mathbb{V})$, shows an energy gap between $\varepsilon = \mathbb{V} + \delta\tau$ and $\varepsilon = \mathbb{V} - \delta\tau$ of width $2\delta\tau$. For energy $0 \leq \varepsilon \leq \frac{\mathbb{V} - \delta\tau}{2}$, the double barrier behaves like a more refractive medium than pristine graphene. On the other hand, for the energy $\frac{\mathbb{V} - \delta\tau}{2} \leq \varepsilon \leq \mathbb{V} - \delta\tau$, it behaves like a less refractive medium and the critical angles are symmetric with respect to $\theta = 0$. The critical angles for energy $\varepsilon \geq \mathbb{V} + \delta\tau$ are also symmetrical and increase as a function of energy in a parabolic way.

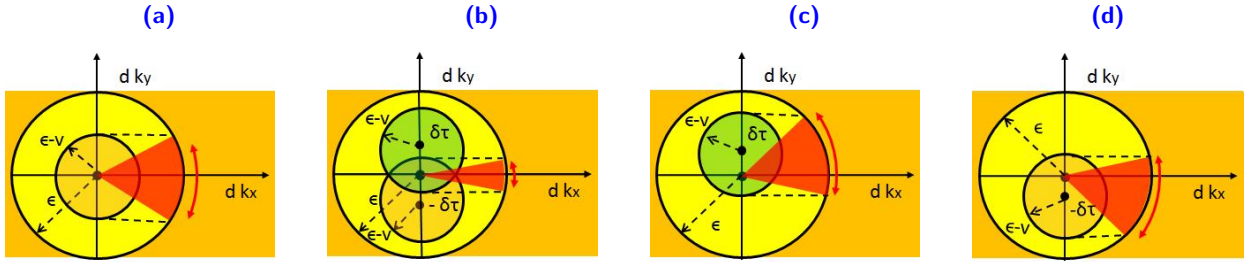


Figure 8 – (color online) Fermi surfaces affected by strain and potential \mathbb{V} in double barrier. (a): $\delta\tau_2 = \delta\tau_4 = 0$. (b): $\delta\tau_2 = -\delta\tau_4 = \pm\delta\tau$. (c): $\delta\tau_2 = \delta\tau_4 = \delta\tau$.

By adding the potential to strained graphene (Figure 8), the Fermi surfaces of each region ② and ④ change their radii and their equations become respectively $(\varepsilon - \mathbb{V})^2 = d^2k_x^2 + (dk_y \pm \delta\tau)^2$ and $(\varepsilon - \mathbb{V})^2 = d^2k_x^2 + (dk_y \pm \delta\tau)^2$. Since the radius becomes variable with the potential \mathbb{V} , Figure 8 generalizes Figure 3. The collimation realized by filtering of certain angles of incidence [3] for different configurations of the double strained barrier, makes it possible to have the contours delimiting the allowed and forbidden transmission zones (red zones) in Figure 8. Figure 8(a) illustrates the behavior of Fermi surfaces for a double barrier without strain, the allowed angles are symmetric with respect to the normal incidence angle and correspond to those of the Figure 7(a). Figure 8(b) illustrates the behavior of the Fermi surfaces for a double barrier with two strains of different nature (one of contraction and the other of compression), the allowed angles have also a symmetry with respect to the normal incidence angle and correspond to those of Figure 7(d). Finally Figure 8(c) (8(d)) shows the Fermi surfaces behavior of a barrier with two strains of the same nature compression (traction). The

displacement of the origin of Fermi surface corresponding to the strained zone, omitted the symmetry with respect to the normal incidence angle. But the permitted angles of Figure 8(c) (compression strain) are symmetrical compared to the allowed angles of Figure 8(d) (traction strain) with respect to the normal angle of incidence.

A geometric manipulation is used to determine easily the limiting angles $\theta_{s'}^s = \arcsin\left(\frac{\mathbb{V}-\varepsilon+s\delta\tau}{s'\varepsilon}\right)$ corresponding to energy contours $\varepsilon_{s'}^s = \frac{\mathbb{V}+s\delta\tau}{1+s'/\sin\theta}$ separating different transmission zones in Figure 8, with $s = \pm$ and $s' = \pm$. These angles are well illustrated in Figure 9 under suitable conditions. Then we have easily obtained such angles delimiting different transmission zones such as $\varepsilon_+^+ \rightarrow \theta_+^+$ (magenta dashed line), $\varepsilon_+^- \rightarrow \theta_+^-$ (brown dashed line), $\varepsilon_-^- \rightarrow \theta_-^-$ (orange dashed line), $\varepsilon_-^+ \rightarrow \theta_-^+$ (green dashed line).

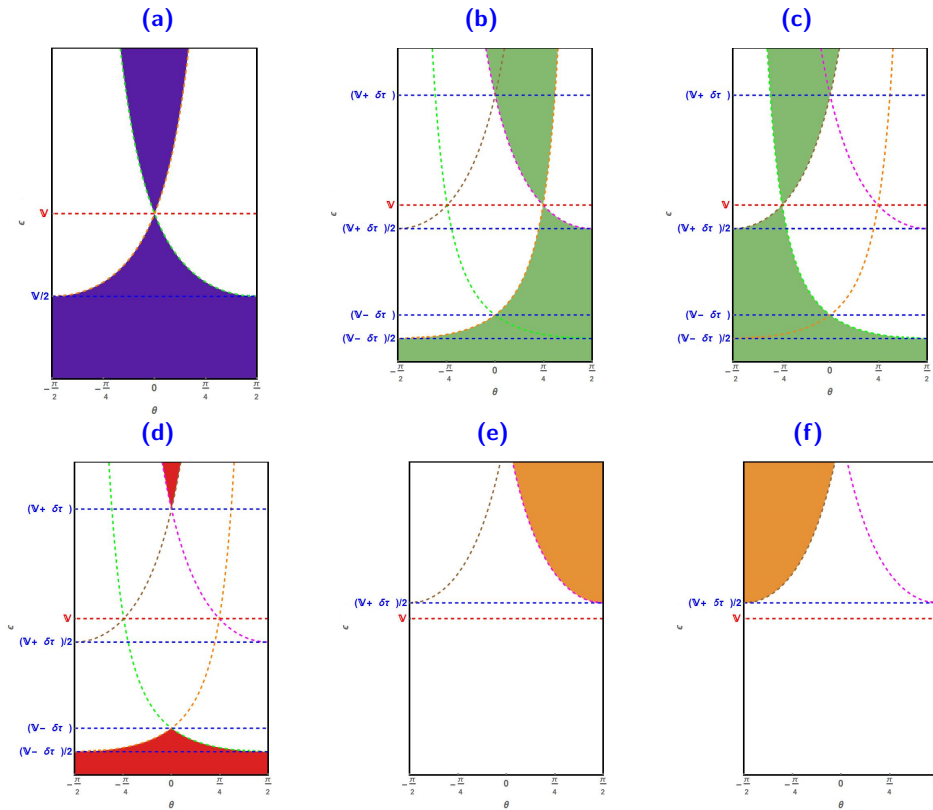


Figure 9 – (color online) Collimation effect on the energy zones, in strained double barrier under the potential profile $(\mathbb{V}_2, \mathbb{V}_4) = (\mathbb{V}, \mathbb{V})$, the forbidden energy zones are white and the allowed energy zones are colored, $\varepsilon_+^+ \rightarrow \theta_+^+ = \arcsin\left(\frac{-\varepsilon+\mathbb{V}+\delta\tau}{\varepsilon}\right)$ (magenta dashed line), $\varepsilon_+^- \rightarrow \theta_+^- = \arcsin\left(\frac{\varepsilon-\mathbb{V}-\delta\tau}{\varepsilon}\right)$ (brown dashed line), $\varepsilon_-^- \rightarrow \theta_-^- = \arcsin\left(\frac{-\varepsilon+\mathbb{V}+\delta\tau}{\varepsilon}\right)$ (orange dashed line), $\varepsilon_-^+ \rightarrow \theta_-^+ = \arcsin\left(\frac{-\varepsilon+\mathbb{V}-\delta\tau}{\varepsilon}\right)$ (green dashed line). (a): $\delta\tau_2 = \delta\tau_4 = \delta\tau = 0$. (b): $\delta\tau_2 = \delta\tau_4 = \delta\tau = 7\pi$. (c): $\delta\tau_2 = \delta\tau_4 = \delta\tau = -7\pi$. (d): $\delta\tau_2 = -\delta\tau_4 = \delta\tau = \pm 7\pi$. (e): $\delta\tau_2 = \delta\tau_4 = \delta\tau = 12\pi$ and $\delta\tau > \mathbb{V}$. (f): $\delta\tau_2 = \delta\tau_4 = \delta\tau = -12\pi$ and $\delta\tau > \mathbb{V}$.

At this level, we show that the corresponding conductance is affected by physical parameters and depends on the nature of system. Indeed, Figure 10 shows the conductance as a function of incident energy ε for different configurations of a strained double barrier which is not subject to any potential, i.e. $(\mathbb{V}_2 = \mathbb{V}_4 = 0)$. In Figures (10(a), 10(b), 10(c)), we present the conductance for strained single barrier ($(\delta\tau_2 = \pm\delta\tau, \delta\tau_3 = \delta\tau_4 = 0)$ or $(\delta\tau_2 = \delta\tau_3 = 0, \delta\tau_4 = \pm\delta\tau)$), double barrier with the same strain ($\delta\tau_2 = \delta\tau_4 = \pm\delta\tau, \delta\tau_3 = 0$) and double barrier with different strains ($\delta\tau_2 = -\delta\tau_4 = \pm\delta\tau, \delta\tau_3 = 0$),

respectively. We observe that under some physical conditions there are conductances for $\delta\tau = 0$ (orange color), $\delta\tau = 3\pi$ (red color), $\delta\tau = 7\pi$ (black color), $\delta\tau = 11\pi$ (blue color) and $\delta\tau = 15\pi$ (green color). These Figures show that each conductance starts at the energy $\varepsilon = \delta\tau$ and there is an ordering such that $G/G_0(\delta\tau = 0) > G/G_0(\delta\tau = 3\pi) > G/G_0(\delta\tau = 7\pi) > G/G_0(\delta\tau = 11\pi) > G/G_0(\delta\tau = 15\pi)$. Figure 10(d) illustrates the comparison between conductances corresponding to strained single barrier (SSB) (blue color) and strained double barriers for both: same strain (SSDB) (red color) and different strains (DSDB) (black color) with $\delta\tau = 7\pi$. Then it is clearly seen that the result G/G_0 (SSB) $>$ G/G_0 (SSDB) $>$ G/G_0 (DSDB) holds.

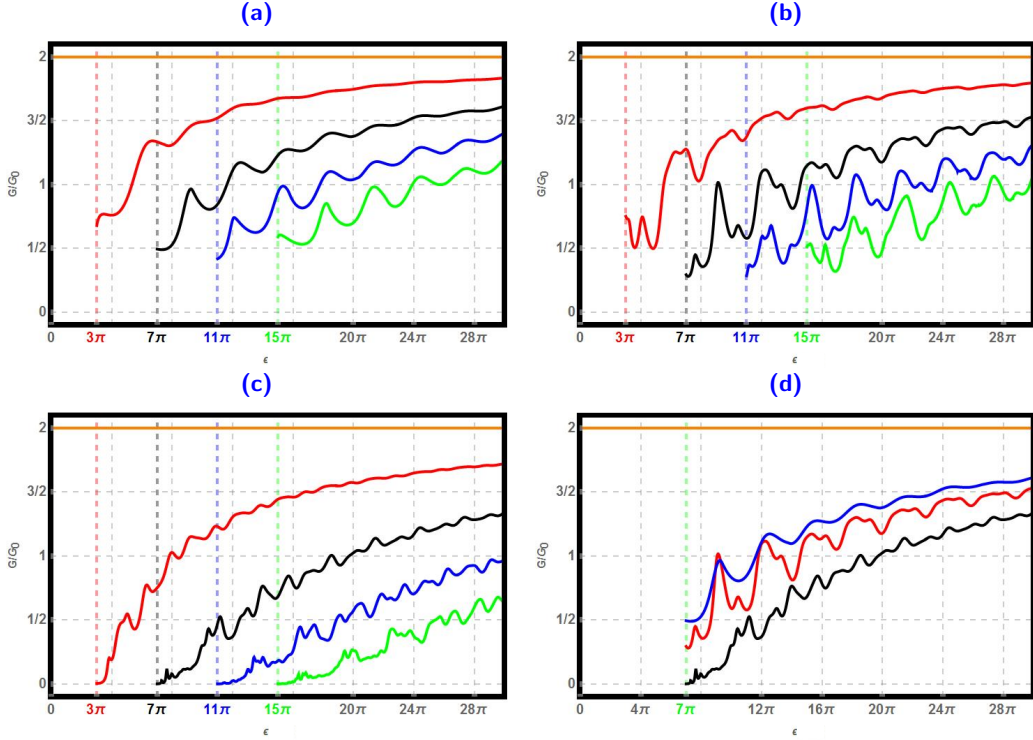


Figure 10 – (color online) Conductance (in units of G_0) $\frac{G}{G_0}$ versus incident energy ε for different configurations of strained double barrier, with $\varrho = 300$, $d = 3\varrho$, $\mathbb{V}_2 = \mathbb{V}_4 = 0$. (a): Strained single barrier with $\delta\tau_2 = \pm\delta\tau, \delta\tau_3 = \delta\tau_4 = 0$ or $\delta\tau_2 = \delta\tau_3 = 0, \delta\tau_4 = \pm\delta\tau$ where $\delta\tau = 0$ (orange line), $\delta\tau = 3\pi$ (red line), $\delta\tau = 7\pi$ (black line), $\delta\tau = 11\pi$ (blue line) and $\delta\tau = 15\pi$ (green line). (b): Strained double barrier with $\delta\tau_2 = \delta\tau_4 = \pm\delta\tau, \delta\tau_3 = 0$ where $\delta\tau = 0$ (orange line), $\delta\tau = 3\pi$ (red line), $\delta\tau = 7\pi$ (black line), $\delta\tau = 11\pi$ (blue line) and $\delta\tau = 15\pi$ (green line). (c): Strained double barrier with $\delta\tau_2 = -\delta\tau_4 = \pm\delta\tau, \delta\tau_3 = 0$ where $\delta\tau = 0$ (orange line), $\delta\tau = 3\pi$ (red line), $\delta\tau = 7\pi$ (black line), $\delta\tau = 11\pi$ (blue line) and $\delta\tau = 15\pi$ (green line). (d): Strained double barrier for $\delta\tau = 7\pi$ in the cases: $(\delta\tau_2 = \delta\tau_4 = \pm\delta\tau, \delta\tau_3 = 0)$ (red line), $(\delta\tau_2 = -\delta\tau_4 = \pm\delta\tau, \delta\tau_3 = 0)$ (black line), $(\delta\tau_2 = \pm\delta\tau, \delta\tau_3 = \delta\tau_4 = 0)$ or $(\delta\tau_2 = \delta\tau_3 = 0, \delta\tau_4 = \pm\delta\tau)$ (blue line).

Figures 11 shows the effect of strain together with applied potential on the conductances with $(\mathbb{V}_2 = \mathbb{V}_4 = 10\pi)$ and $(\mathbb{V}_2 = 10\pi, \mathbb{V}_4 = 0$ or $\mathbb{V}_2 = 0, \mathbb{V}_4 = 10\pi)$. We observe that the behavior of the conductance changed absolutely compared to Figure 10. The strainless double barrier conductance in Figures 11(b), 11(c), 11(d) and single barrier conductance in Figure 11(a) (orange color) have even minimum located at $\varepsilon = \mathbb{V} = 10\pi$. These two conductances differ in resonance peaks, which due to the double barrier (Fabry-Perot resonator model). Figures 11(a) (SSB) and 11(b) (SSDB) show that the conductances, for $\delta\tau = 0$ (orange color), $\delta\tau = 3\pi$ (red color), $\delta\tau = 7\pi$ (black color), are almost comparable in values and only differ in their mass terms corresponding to the limit of the forbidden

zones, respectively, $\varepsilon = 0, 3\pi$ and 7π . But the conductances for $\delta\tau = 11\pi$ (blue color) and $\delta\tau = 15\pi$ (green color) remain separated and only differs by oscillations. In Figure 11(c) of DSDB the three conductances fell at energy $\varepsilon = \mathbb{V} = \delta\tau$ until the value zero, then they resume after an increase in energy. A comparison between the three kinds of strained double barriers subject to a potential \mathbb{V} is illustrated in Figure 11(c). The conductance of SSB has the same minimum as that of simple potential barrier $\mathbb{V} = 10\pi$ at $\varepsilon = \mathbb{V} = 10\pi$, but the conductance of the SSDB and DSDB start with zero at $\varepsilon = \mathbb{V} = \delta\tau$. By increasing their Fermi energies, SSB resumes its conductance before DSDB.

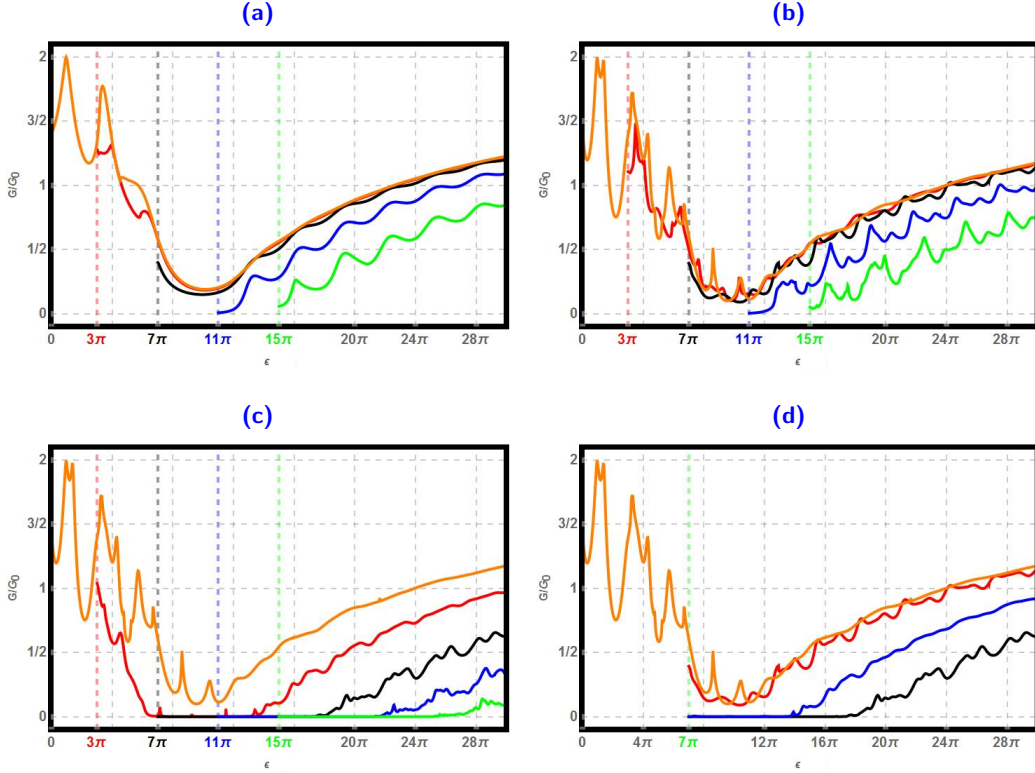


Figure 11 – (color online) Conductance (in units of G_0) $\frac{G}{G_0}$ versus incident energy for different configurations of strained double barrier, ε with $\varrho = 300$, $d = 3\varrho$ and ($\mathbb{V}_2 = \mathbb{V}_4 = 10\pi$). (a): Strained single barrier, ($\delta\tau_2 = \pm\delta\tau, \delta\tau_3 = \delta\tau_4 = 0$) or ($\delta\tau_2 = \delta\tau_3 = 0, \delta\tau_4 = \pm\delta\tau$) where $\delta\tau = 0$ (orange line), $\delta\tau = 3\pi$ (red line), $\delta\tau = 7\pi$ (black line), $\delta\tau = 11\pi$ (blue line) and $\delta\tau = 15\pi$ (green line). (b): Strained double barrier with ($\delta\tau_2 = \delta\tau_4 = \pm\delta\tau, \delta\tau_3 = 0$) where $\delta\tau = 0$ (orange line), $\delta\tau = 3\pi$ (red line), $\delta\tau = 7\pi$ (black line), $\delta\tau = 11\pi$ (blue line) and $\delta\tau = 15\pi$ (green line). (c): Strained double barrier with ($\delta\tau_2 = -\delta\tau_4 = \pm\delta\tau, \delta\tau_3 = 0$) where $\delta\tau = 0$ (orange line), $\delta\tau = 3\pi$ (red line), $\delta\tau = 7\pi$ (black line), $\delta\tau = 11\pi$ (blue line) and $\delta\tau = 15\pi$ (green line). (d): Strained double barrier for $\delta\tau = 7\pi$ in case: ($\delta\tau_2 = \delta\tau_4 = \pm\delta\tau, \delta\tau_3 = 0$) (red line), ($\delta\tau_2 = -\delta\tau_4 = \pm\delta\tau, \delta\tau_3 = 0$) (black line), ($\delta\tau_2 = \pm\delta\tau, \delta\tau_3 = \delta\tau_4 = 0$) or ($\delta\tau_2 = \delta\tau_3 = 0, \delta\tau_4 = \pm\delta\tau$) (blue line).

5 Conclusion

We have studied the electronic structure of Dirac fermions through a double barrier potential in a strained graphene ribbon. Our system is a graphene chip made up of five regions where the second and fourth subjected to the strain effect and double barrier potential. In such system the armchair configuration along the x -direction imposes a gauge field \mathcal{A}_j perpendicular to the direction of propagation, which only affected horizontal inter-carbon links. After writing the Hamiltonian governing Dirac

fermions in each region, we have determined the energies spectrum and associated eigenspinors. It was shown that the transverse wave vector is shifted by the strain term compared to that of the pristine graphene and the strain directly affects the transmission angle of Dirac fermions. The continuity of the eigenspinors at each interface separating two consecutive regions, allowed us to build a transfer matrix connecting the amplitudes of propagation in the *input* and *output* regions. We have calculated the transmission and reflection probabilities together with the conductance at zero temperature.

Subsequently, we have numerically presented the transmission probability density plots versus the incident energy ε and incident angle θ under suitable conditions. These density plots showed the forbidden and permitted zones of transmission delimited by the energy contours $\varepsilon = \frac{\delta\tau}{1 \pm \sin\theta}$, where Klein paradox zones are highlighted in red (total transmission), transmission gaps in purple and forbidden zones in white in all generated Figures. It has been seen that the Klein paradox is not always verified at normal incident angle and the transmissions satisfy three symmetry relations related to the incident angle and strain effect (deformation), see (23a-23c). The Fermi surfaces, corresponding to the dispersion relation, allowed us to determine the collimation angles for different configurations of the strain effect and double barrier. These angles can also be obtained using the conservation of the k_y wave-vector component throughout the Dirac fermions propagation. We have showed that the transmission probability exhibited double resonance peaks, which can be explained by Fabry-Perot resonator model. At grazing incidence angle $\theta = \frac{\pi}{2}$, we have seen that the transmission showed only resonance peaks and transmission gaps.

By considering double barrier potential together with strain effect, we have showed that the transmission behavior changed completely. Indeed, the allowed and forbidden zones of transmission were now delimited by energy contours $\varepsilon_{s'}^s = \frac{V+s\delta\tau}{1+s'\sin\theta}$ with $s = \pm$ and $s' = \mp$. Always under the conservation constraint of the k_y wave-vector component, and taking into account the Fermi surfaces, we have the following correspondences between the delimiting energies contours and the collimation angles: $\varepsilon_{s'}^s = \frac{V+\alpha\delta\tau}{1+s'\sin\theta} \rightarrow \theta_{s'}^s = \arcsin\left(\frac{V-\varepsilon+s\delta\tau}{s'\varepsilon}\right)$ Finally, we have performed a comparative study of the conductances between different configurations of strained double barrier with or without potential profile.

Acknowledgments

The generous support provided by the Saudi Center for Theoretical Physics (SCTP) is highly appreciated by all authors. AJ and HB acknowledge the support of KFUPM under research group project RG181001.

References

- [1] J. Scott Bunch, Arend M. van der Zande, Scott S. Verbridge, Ian W. Frank, David M. Tanenbaum, Jeevak M. Parpia, Harold G. Craighead, Paul L. McEuen, Science 315, 490 (2007).
- [2] N. Levy, S. A. Burke, K. L. Meaker, M. Panlasigui, A. Zettl, F. Guinea, A. H. Castro Neto, M. F. Crommie, Science 329, 544 (2010).
- [3] V. M. Pereira and A. H. Castro Neto, Phys. Rev. Lett. 103, 046801 (2009).

- [4] F. Guinea, M. I. Katsnelson and A. K. Geim, *Nat. Phys.* 6, 30 (2010).
- [5] F. De Juan, A. Cortijo, M. A. H. Vozmediano, A. Cano, *Nat. Phys.* 7, 810 (2011).
- [6] K. S. Novoselov, A. K. Geim, S. V. Morozov, D. Jiang, Y. Zhang, S. V. Dubonos, I. V. Grigorieva and A. A. Firsov, *Science* 306, 666 (2004).
- [7] K. S. Novoselov, A. K. Geim, S. V. Morozov, D. Jiang, M. I. Katsnelson, I. V. Grigorieva, S. V. Dubonos and A. A. Firsov, *Nature* 438, 197 (2005).
- [8] Yuanbo Zhang, Yan-Wen Tan, Horst L. Störmer and Philip Kim, *Nature* 438, 201 (2005).
- [9] A. H. Castro Neto, F. Guinea, N. M. R. Peres, K. S. Novoselov, and A. K. Geim, *Rev. Mod. Phys.* 81, 109 (2009)
- [10] H. Bahlouli, E. B. Choubabi, A. Jellal, and M. Mekkaoui, *J. Low Temp. Phys.* 169, 51 (2012).
- [11] C. Yesilyurt, S. Ghee Tan, G. Liang, and M. B. Jalil, *AIP Advances* 6 (5), 056303 (2016).
- [12] M. Büttiker, Y. Imry, R. Landauer, and S. Pinhas, *Phys. Rev. B* 31, 6207 (1985).
- [13] X. Xia, J. Wang, F. Zhang, Z. D. Hu, C. Liu, X. Yan, and L. Yuan, *Plasmonics*, 10, 6, 1409(2015).
- [14] N. Gu, M. Rudner, and L. Levitov, *Phys. Rev. Lett.* 107, 156603 (2011).
- [15] A. Daboussi, L. Mandhour, J. N. Fuchs, and S. Jaziri, *Phys. Rev. B* 89, 085426 (2014).
- [16] S. Li-Feng, D. Li-Min, W. Zhi-Fang, and F. Chao, *Chinese Phys. B* 22, 077201 (2013).
- [17] N. M. R. Peres, A. C. Neto, and F. Guinea, *Phys. Rev. B* 73, 195411 (2006).